The Planetary Science Journal, 6:49 (11pp), 2025 February https://doi.org/10.3847/PSJ/ada6aa

Vertical and Temporal H_3^+ Structure at the Auroral Footprint of Io

A. Mura[1], A. Moirano[1,2], V. Hue[3], C. Castagnoli[1,4,5], A. Migliorini[1], F. Altieri[1], A. Adriani[1], A. Cicchetti[1], C. Plainaki[6], G. Piccioni[1], R. Noschese[1], G. Sindoni[6], and R. Sordini[1]
[1] Institute for Space Astrophysics and Planetology, National Institute for Astrophysics, Roma, Italy
[2] Laboratory for Planetary and Atmospheric Physics, Space Sciences, Technologies and Astrophysical Research Institute, University of Liège, Liège, Belgium
[3] Aix-Marseille Université, CNRS, CNES, Institut Origines, LAM, Marseille, France
[4] University of Rome "Tor Vergata," Roma, Italy
[5] ISAC-CNR, Bologna, Italy
[6] Agenzia Spaziale Italiana, Rome, Italy
Received 2024 October 15; revised 2024 December 17; accepted 2025 January 3; published 2025 February 21

Abstract

We report the first observation of the vertical and temporal structure of the H_3^+ emission at the auroral footprint of Io, as observed by Juno/JIRAM. The brightness vertical profile shows a maximum at 600 km above 1 bar, with no apparent difference between the main Alfvén wing (MAW) spot emission and the tail of the footprint. This observation better aligns with a broadband energy distribution of the precipitating electrons, instead of a monoenergetic one. The temporal profile of H_3^+ column density has been observed after the passage of the MAW and shows a hyperbolic decrease. A model of H_3^+ decay is proposed, which takes into account the second-order kinetics of dissociative recombination of H_3^+ ions with electrons. The model is found to be in very good agreement with Juno observations. The conversion factor from radiance to column density has been derived, as well as the half-life for H_3^+, which is not constant but inversely proportional to the H_3^+ column density. This explains the wide range of H_3^+ lifetimes proposed before.

Unified Astronomy Thesaurus concepts: Near infrared astronomy (1093); Jupiter (873); Aurorae (2192)

1. Introduction

The infrared emission spectrum of H_3^+ was first discovered by T. Oka (1980); a few years later, P. Drossart et al. (1989) identified such emission from Jupiter's atmosphere. They proposed that the formation of H_3^+ was due to the ionization from electron precipitation and photoionization of neutral H_2 molecules, which then quickly react with neutral H_2 to form H_3^+ and H ($H_2 + H_2^+ \rightarrow H_3^+ + H$). The reaction is highly exothermic, so that a considerable amount of heat is deposited in the atmosphere with this reaction. P. Drossart et al. (1989) also proposed that this process could occur in the upper atmosphere of Jupiter ($h > 500$ km) because, at that altitude, H_3^+ emission is very intense, while the radiation from the deeper Jupiter's atmosphere is shielded by the more abundant methane layer, at ~200 km (J. E. P. Connerney & T. Satoh 2000). Because of the correlation with electron precipitation, J. E. P. Connerney & T. Satoh (2000) proposed to use such emission as a diagnostic tool to study the magnetosphere of Jupiter, and, for this purpose, the NASA mission Juno to Jupiter (S. J. Bolton et al. 2017) is equipped with a dedicated instrument, the Jovian InfraRed Auroral Mapper (JIRAM; A. Adriani et al. 2008, 2017a). The JIRAM scientific goals are to explore the Jovian aurorae and the planet's atmospheric structure, dynamics, and composition. JIRAM images and spectra of the H_3^+ emission have shown the auroral regions of Jupiter with unprecedented detail, observing the northern and southern aurorae 2 hr apart (A. Adriani et al. 2017b; B. M. Dinelli et al. 2017; M. L. Moriconi et al. 2017; A. Mura et al. 2017). Outside of the main oval, JIRAM also provided measurements of the auroral emissions coming from the electromagnetic interactions between Jupiter and its moons (A. Mura et al. 2018; A. Moirano et al. 2021, 2023). Compelling features of Jupiter's aurora, and absent at Earth, these emissions are located at the magnetic footprints of the Galilean moons Io, Europa, and Ganymede (J. E. P. Connerney et al. 1993, J. T. Clarke et al. 1996, P. Zarka, 2004). They stem from the interactions between the moons and the corotating magnetized plasma that fills the extended space environment, or magnetosphere, of this giant planet. Several processes are proposed to explain these auroral features. One theory evokes plasma (Alfvén) waves that travel from the moon to Jupiter's northern and southern high-latitude regions, along the magnetic field (F. Neubauer, 1980, M. H. Acuña et al. 1981, J. W. Belcher et al. 1981, M. Kivelson et al. 2004), bouncing between hemispheres (D. A. Gurnett and C. K. Goertz 1981), and accelerating electrons as they proceed both toward and away from Jupiter along the magnetic field lines (e.g., S. L. G. Hess et al. 2010). Electrons precipitating into the Jovian atmosphere produce hydrogen emissions associated with the moon−magnetosphere interaction, equatorward of the main auroral oval (Bertrand Bonfond et al. 2017). Juno infrared and UV observations of the moon-generated auroral features (A. Mura et al. 2018, J. R. Szalay et al. 2018; A. Moirano et al. 2021, 2023; V. Hue et al. 2022, 2023, J. Rabia et al. 2023, J. Rabia et al. 2024) show many more structures than anticipated from Earth-based observations. By using JIRAM images, A. Mura et al. (2018) found that the footprint feature has a quite complex morphology with multiple small dots arranged in a zig-zag pattern, like a von Kármán vortex street (T. von Kármán, 1911), eventually turning into a turbulent tail. They also noted that the timescale for the decay of the intense H_3^+ emission of these features was shorter (~60 s) than the typical timescale for H_3^+ destruction (~1000 s; T. Stallard et al. 2002) proposed earlier.

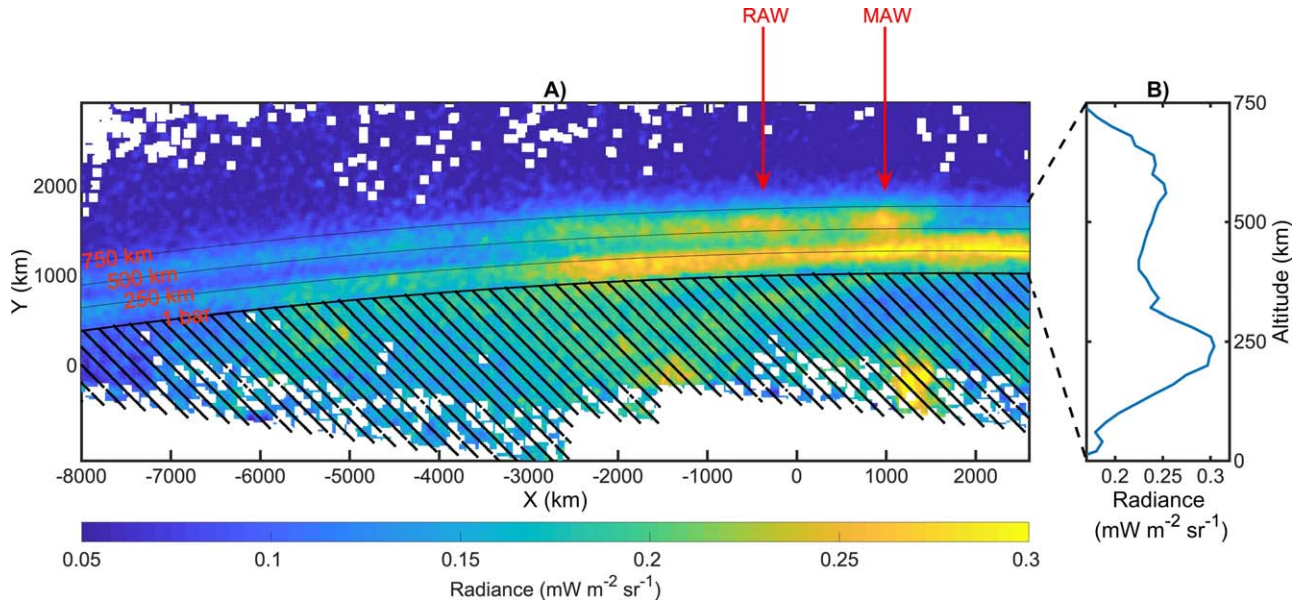

Figure 1. (a) H_3^+ emission from Io's auroral footprint (north) as seen at limb, created using 32 *L*-band (3.3–3.6 μm) images from orbit 31 (2012 December 30). The *x*- and *y*-axes show distances in kilometers (arbitrary origin of axis), with four curved lines indicating Jupiter's 1 bar pressure level and altitudes of 250, 500, and 750 km (red labels). The cross-hatched region represents the region below the 1 bar level. Radiance intensity, mainly from H_3^+, peaks at approximately 600–650 km, with an emitting column 100–200 km high. Methane emission (not related to Io) is visible near 250 km. MAW and RAW spots are indicated by the red arrows. Close to the location of the RAW, a TEB can also contribute to the emission. The predicted location of the MAW is ahead of the observed MAW by about 1000 km, using the lead-angle model by V. Hue et al. (2023). (b) Zoom-in on radiance intensity between 0 and 750 km, calculated on a column corresponding to the main spot.

Knowing the decay rate of H_3^+ is crucial for understanding the comparative analysis of UV and IR images of Jupiter's aurora, as it helps to accurately interpret the temporal and spatial differences in the two bands (J.-C. Gérard et al. 2018). As noted by C. Tao et al. (2011, Equation (9) for $P = 0$), the reaction rate depends on the square of the density. In such reactions, known as second-order chemical kinetics, the classic exponential decay does not apply; therefore, as shown in this study, the definition of an H_3^+ lifetime can be misleading, as it depends on the H_3^+ density. Density varies with altitude and reaches a maximum around 600 or 700 km above 1 bar (A. Migliorini et al. 2023). Consequently, the H_3^+ decay follows a complex pattern, and an accurate modeling of the vertical profile is necessary to obtain precise results. In this study, we first derive the vertical profile of H_3^+ emission, and then apply it to a model of H_3^+ decay. Finally, we compare the model with data.

In Section 2, we describe the vertical structure of Io's auroral footprint. Section 3 presents data on the temporal variability of secondary spots. In Section 4, we outline the model and conduct the analysis. A summary and conclusions are provided in Section 5. The instrument and data set are detailed in Appendices A1 and A2, respectively.

2. Vertical Profile

In Figure 1 we present the first detailed image of the vertical profile of Io's auroral footprint emission, observed in the north. Previously, footprint images taken at the limb were produced, including those acquired by the Hubble Space Telescope (HST). However, none were captured at this level of detail, which allows for an accurate reconstruction of the vertical profile. Figure 1 was created using 32 images taken over the northern Io auroral footprint during orbit 31, on 2012 December 30, from 21:05 to 21:25 (see Appendix A2 for a table of the observations). These images represent *L*-band radiance, integrated from 3.3 to 3.6 μm. The images were projected onto a plane defined by three points: the origin at the center of Jupiter, the estimated location of Io's footprint at the start of the observation, and the estimated location of Io's footprint at the end of the observation. By assuming that the H_3^+ emission originates from this plane, or close to it, we determine the height relative to the 1 bar pressure level. Since we assume that the footprint emission is localized, this approach avoids the need to develop an "onion-peeling" model. A minor source of error arises from possible deviation of the actual location of the footprint with respect to the estimated one. Here we use the model by J. E. P. Connerney et al. (2018) to perform the estimation of the footprint position and the lead-angle model by Hue et al. (2023).

The *x*- and *y*-axes of the figure represent distances in kilometers relative to an arbitrary point. The four curved lines in the figure represent Jupiter's 1 bar pressure level and three other levels at 250, 500, and 750 km. Both the main Alfvén wing (MAW) and the reflected Alfvén wing (RAW) (B. Bonfond et al. 2008, 2009, 2010) spots are clearly visible in the mosaic and are indicated by the red arrows. At the same location of the RAW, a trans-hemispheric electron beam (TEB; B. Bonfond et al. 2008) can also contribute to the emission. Depending on Io's centrifugal latitude, the TEB is sometimes ahead of the MAW, sometimes following it. In this case, the predicted location is in fact the same as that of the RAW (Moirano et al. 2023).

Panel (b) zooms in on the intensity of radiance as a function of altitude, between 0 and 750 km, with the highest intensity roughly corresponding to the main spot. The radiance intensity, originating from H_3^+, peaks at approximately 600 km; the height of the column of emitting H_3^+ is approximately 100 or 200 km.

At 3.3 μm, mixed with the substantial H_3^+ emission, weaker emission due to methane has been observed in the auroral emission (A. Adriani et al. 2017b; B. M. Dinelli et al. 2017;

M. L. Moriconi et al. 2017) when observed vertically. The emission near 250 km can be attributed to methane (hence, it is not related to Io), as shown by A. Migliorini et al. (2023). The emission from CH_4 looks more intense than the one coming from H_3^+, just because it is seen tangentially and not from above as usual, i.e., the line of sight is much longer for CH_4. In any case, this emission is separable from the H_3^+ emission. There may also be a background auroral emission that cannot be eliminated or removed from this figure. In summary, it is quite clear that the dominant emission in the region between 500 and 750 km is from H_3^+.

3. Time Evolution of H_3^+ Emission from the Footprint of Io

A. Mura et al. (2018) showed that the auroral footprint of Io (IFP) consists not only of the well-known MAW, RAW, and TEB but also of a series of secondary spots that follow the MAW in Io's footprint ("sub-dots"). A. Moirano et al. (2021) analyzed these sub-dots and demonstrated that they are stationary in the SIII reference frame (i.e., in the Jovian ionosphere). The cause of these spots remains unclear; as noted by S. Schlegel & J. Saur (2022), multiple physical interpretations are possible.

Nonetheless, the most straightforward interpretation is that these spots are formed following the passage of the MAW, due to transient electron precipitation (the physical reason why this electron precipitation may be pulsating remains unclear, but it is not relevant for this study). After the passage of the MAW, we observe a stationary but dimming sub-dot, due to the disappearance of H_3^+ caused by recombination with electrons.

With this premise, and acknowledging that we cannot entirely rule out subsequent electron precipitation, we produce maps of the *L*-band radiance of the south IFP at 30 s time steps; we also define a region of interest (ROI) of 200 × 200 km over one of the sub-dots. We then calculate the average radiance within the ROI, ensuring that a single stable sub-dot remains within this region.

A. Moirano et al. (2021) presented a very long sequence of 16 images (i.e., ∼8 minutes), as shown in Figure 3 of that study, in which sub-dots are stationary, and they excluded the possibility of sub-dot motion that occurs on timescales in between the observations (every 30 s). However, there are at least two reasons why we prefer to avoid analyzing such long sequences. The first reason is that the RAW (or sometimes a TEB), following the MAW, would eventually enter the ROI, compromising the analysis, which relies on the absence of any other electron precipitation in the area during the study. The second reason is due to ionospheric winds, which can reach speeds of the order of 1 km s^{-1} at the height of H_3^+ (J. P. Maillard et al. 1999; D. Rego et al. 1999; T. Stallard et al. 2001; R. E. Johnson et al. 2017). To avoid potential blurring caused by these winds, it is preferable to limit the analysis to sequences shorter than 200 s (that is, the size of the ROI divided by the speed of winds).

The JIRAM database contains several useful examples; we focus on the two best: one from orbit 13 and the other from orbit 26. The first example is illustrated in Figure 2, with further details provided in the Appendix. Seven orthographic maps of *L*-band radiance, detected by JIRAM and projected to a level of 650 km, are shown. Images were acquired at approximately 30 s intervals over a total duration of 3 minutes. The radiance is corrected for the emission angle (e) with a cosine law—that is, we divide by cos(e) to take into account the longer line of sight for slant observations. The ROI is represented by the red square; the mean value of the radiance in the ROI is given in Table A2. A second data set, obtained from orbit 26, provides eight useful images and is described in Table A3.

4. Theory and Modeling

4.1. Formation and Destruction of H_3^+

H_3^+ is predominantly formed at altitudes ranging from 500 to 1000 km, with its maximum concentration occurring around 600 to 700 km above the 1 bar pressure level. In the model proposed by C. Tao et al. (2011), this peak is calculated as a function of the energy of the electron beam (E), and it is below 1000 km for $E > 1$ keV and at about 700 km for $E = 10$ keV (refer to their Figure 6(b)). Other studies have observed the maximum H_3^+ emission at approximately 700–900 km and 680–950 km for H_3^+ overtone (a vibrational transition in a molecule where the vibrational quantum number changes by more than one unit) and hot overtone emissions in the northern auroral region (M. B. Lystrup et al. 2008; T. Uno et al. 2015). H. Watanabe et al. (2018), who utilized the same model as C. Tao et al. (2011), found that the peak altitudes for electrons with energies of 1, 10, 30, 100, and 300 keV are 1400, 770, 600, 560, and 560 km above the 1 bar level, respectively. In nonauroral, midlatitude regions, H_3^+ emission occurs at altitudes between 300 and 500 km above the 1 bar level (T. S. Stallard et al. 2015, using Cassini/VIMS data; A. Migliorini et al. 2019, using Juno/JIRAM data). Additionally, A. Migliorini et al. (2023) present limb observations from JIRAM data, reporting detached infrared emissions from both H_3^+ and methane. This finding supports our assumption that H_3^+ emission can be effectively isolated in JIRAM data.

Finally, in the previous section, we estimate the H_3^+ peak emission altitude in the specific auroral footprint region (which is the most appropriate quantity here) as 600 or 650 km with good accuracy. At these altitudes, in any case, vibrational local thermal equilibrium (LTE) can generally be assumed (H. Melin et al. 2005, B. M. Dinelli et al. 2017). This means that the vibrational temperature closely matches that of the thermosphere/ionosphere (i.e., H. A. Lam et al. 1997; S. Miller et al. 1997). The peak of auroral production of H_3^+ is observed at 600–650 km, where the atmosphere consists primarily of neutral H_2 (N. Achilleos et al. 1998; C. Tao et al. 2011). By comparing in-between collision time and the typical time before emission from H_2 and H_3^+, T. Stallard et al. (2002) concluded that LTE is a reasonable assumption for the region where H_3^+ emits. Similarly, C. Tao et al. (2011) found that non-LTE fraction becomes negligible below 1000 km.

The interaction of charged particle precipitation with Jupiter's H_2-dominated atmosphere leads to auroral emission from H_2 and H in the far-UV (J. T. Clarke et al. 1996, 1998; S. V. Badman et al. 2015), which is another diagnostic tool for the magnetosphere of Jupiter. There is also some emission in the visible range (A. P. Ingersoll et al. 1998; A. R. Vasavada et al. 1999). Auroral UV emission reflects the immediate energy input from impacting electrons, while IR emission shows the atmospheric response through heating and energy deposition (J.-C. Gérard et al. 2018). The neutral atmosphere quickly thermalizes the H_3^+ ions after their formation. If LTE assumption is correct, then it is possible to infer the thermosphere temperature by modeling the relative strength of H_3^+

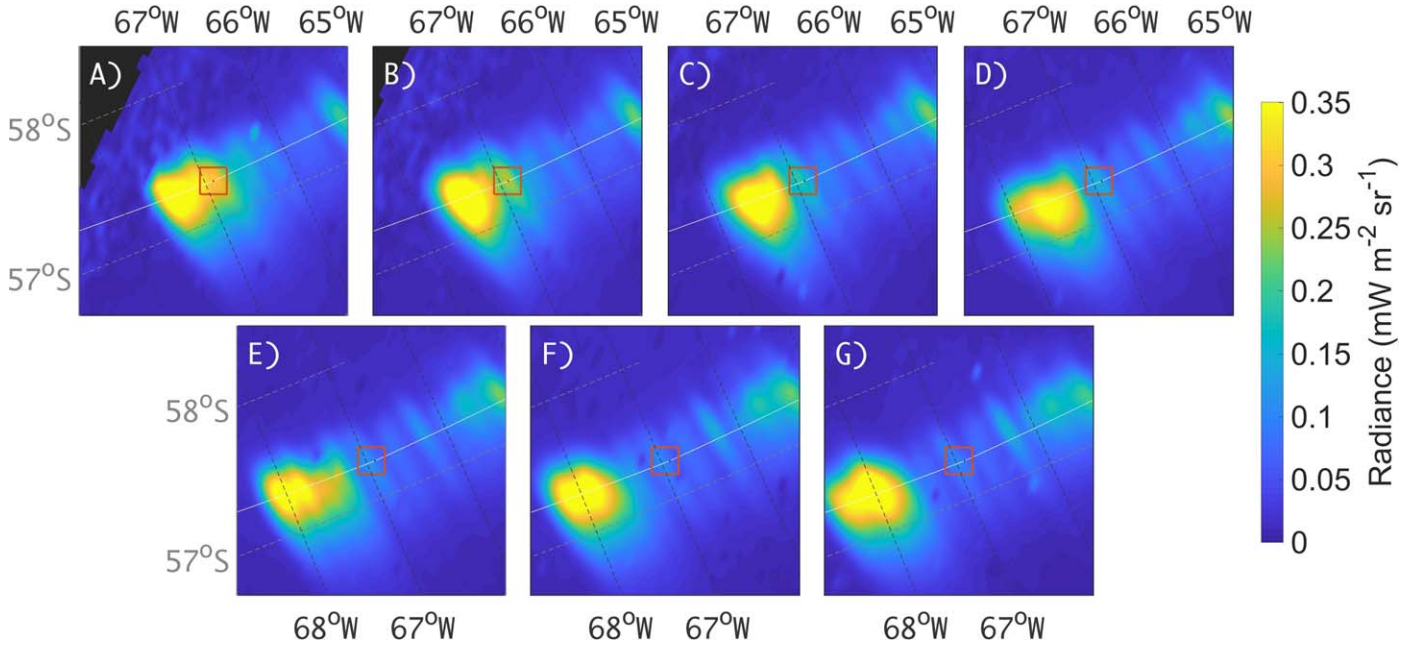

Figure 2. Seven observations (radiance maps in the *L* band) of the south IFP taken during Juno's orbit 13 (taken from 07:12:30 to 07:15:30 on 2018 May 24, at intervals of ∼30 s). The red square is the ROI used to calculate the mean radiance from a fixed ionospheric column. The white line is the trajectory of the IFP predicted by the model of J. E. P. Connerney et al. (2018). The dashed lines are meridians (67° and 68° west) and parallels (57° and 58° south).

roto-vibrational lines (B. M. Dinelli et al. 1992, 1995, 2017; H. A. Lam et al. 1997; T. Stallard et al. 2002). In summary, H_3^+ IR emission can be used to derive both the atmospheric temperature and integrated column, thus allowing the mapping of the ion distribution (B. M. Dinelli et al. 2017).

The H_3^+ is formed by the reaction

$$H_2 + H_2^+ \rightarrow H_3^+ + H.$$

The reaction rate is 2×10^{-9} cm^3 s^{-1} (J. J. Perry et al. 1999), and since the H_2 density below 1000 km exceeds 10^{10} cm^{-3}, any H_2^+ quickly results in a H_3^+ molecule. The newly produced H_3^+ is in an excited state and immediately decays with the production of IR radiation. The excited states are continuously refilled via collisions, so that H_3^+ emits in the IR until it is destroyed. The recombination with hydrocarbons is the main destruction channel at low altitudes (∼less than 500 km), while the electron recombination dominates above the methane homopause:

$$H_3^+ + e \rightarrow H + H + H \text{ or } (H_2 + H)$$
$$H_3^+ + CH_4 \rightarrow CH_5^+ + H_2.$$

4.2. Decay Rate of H_3^+

The density and temperature of ionospheric electrons can be assumed to be the same as those of H_3^+ (J. H. Waite et al. 1983; C. Tao et al. 2011). Therefore, after the passage of the electron precipitation associated with the MAW spot over a given area of Jupiter's atmosphere, the local concentration of H_3^+ decays according to the following differential equation:

$$\frac{dn_{H_3^+}}{dt} = -k n_{H_3^+}{}^2 \quad (1)$$

(see also Equation (9) in C. Tao et al. 2011). The value of k for the destruction rate has been repeatedly questioned (see S. Miller et al. 2020, and references therein); a critical review of the experiments that measured k and its uncertainty is provided by M. Larsson et al. (2008) and M. Larsson (2012). Here we adopt the formula given by G. Sundström et al. (1994):

$$k = 1.15 \times 10^{-7} \left(\frac{300}{T_e}\right)^{0.65}, \quad (2)$$

where k is given in cm^3 s^{-1} and T_e is the electron temperature, in K. We note that this same value is used by C. Tao et al. (2011), and hence by H. Watanabe et al. (2018), since their cited reference (J. J. Perry et al. 1999) inherits the work of G. Sundström et al. (1994); the consistency between published studies justifies the choice of this value.

At the altitude of the IFP emission observed in Figure 1, we can neglect the destruction of H_3^+ by CH_4 since the rate (2.4×10^{-9} cm^3 s^{-1}; S. K. Atreya and T. M. Donahue 1975; W. T. Huntress 1975; T. W. Huntress 1977) is 10 times lower than k, so that this reaction is only effective when n_{CH_4} is larger than $n_{H_3^+}$, which is not the case at $h > 500$ km (see a review of n_{CH_4} vertical profiles in A. Sánchez-López et al. 2022).

The solution of the differential Equation (1) can be easily obtained by separation of variables and is

$$n_{H_3^+} = \frac{1}{c + kt} \quad (3)$$

for $t = 0$, $n_{H_3^+} = 1/c$; hence, c is a parameter that has the dimensions of cm^3 and is the inverse of the H_3^+ density at $t = 0$. The process described here, where the rate of change is proportional to the square of the concentration, is known as "second-order kinetics" (or a "second-order reaction" in chemistry) and is common in reactions where two reactant molecules need to collide for the reaction to occur and the reaction rate depends on the concentration of both. The term "hyperbolic decay" can be used to describe how the

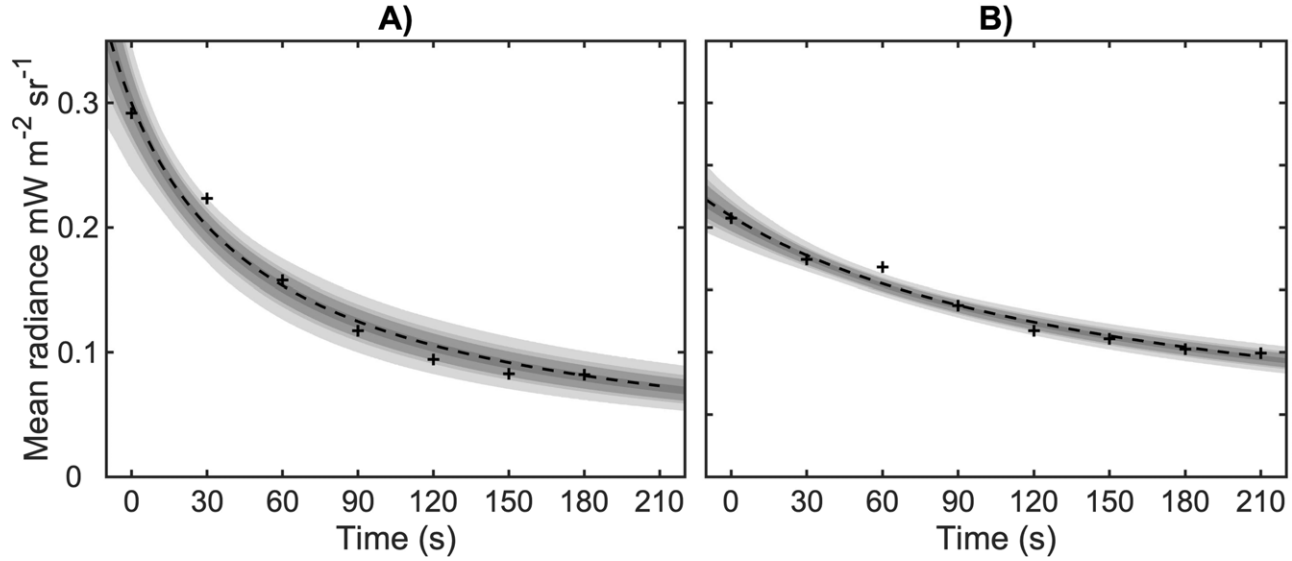

Figure 3. Temporal variability for the mean radiance within the ROI for (a) orbit 13 and (b) orbit 26. The dashed line represents the best-fit function. The gray regions represent the density plot from the MCMC model, which is representative of the model uncertainty.

concentration decreases over time for second-order processes, as opposed to the exponential decay seen in first-order kinetics. Second-order kinetics are commonly seen in bimolecular reactions, such as two molecules of the same or different species reacting together.

To obtain the radiance in the L band, it is sufficient to integrate $n_{H_3^+}$ along the line of sight. A factor f transforms the H_3^+ column density into L-band radiance (R_L):

$$R_L = f \int n_{H_3^+} dl, \tag{4}$$

where f depends on the Einstein coefficients for spontaneous emission associated with the H_3^+ transitions in the L band and the thermospheric temperature. We intentionally consider f as a free parameter to the fit performed in the next section, and we will then check whether we obtain realistic values for f and for the column density. The value for f is intended as an average for the whole column, as the variability of f due to thermospheric temperature is not included. The thermospheric temperature is not directly measured in this region but rather modeled (see J. N. Yates et al. 2020). However, implementing the variability of f does not sensibly improve the results (see Appendix A2 "Methods").

4.3. Model and Data Analysis

The model to reproduce the decay of the radiance observed in Figure 2 is obtained by assuming, for simplicity, that, at the initial instant $t = 0$, the vertical profile of H_3^+ follows a Gaussian distribution. This distribution peaks at 600 km with a sigma of 100 km, consistent with the data presented in Figure 1(b). The Gaussian form is described by

$$n_{H_3^+}(t = 0) = n_p e^{-\frac{(h-600)^2}{2\times 100^2}}, \tag{5}$$

where h represents the altitude above the 1 bar pressure level, measured in km, and n_p denotes the peak density at 600 km and at $t = 0$. By combining this expression (Equation (5)) with the previous ones, we obtain the H_3^+ density as a function of time.

Table 1
Best-fit Parameters and Reduced χ^2 Values for the MCMC Model

Orbit	n_p (cm^{-3})	f (10^{-18} W m^{-2} sr^{-1} cm^2)	χ^2/ν (mW m^{-2} sr^{-1})
13	3.7×10^5	40	1×10^{-3}
26	1.3×10^5	80	3×10^{-4}

Further, using this result in Equation (4) allows us to estimate the radiance generated by the column, directed upward.

The value of k is calculated as a function of the altitude using Equation (2) and using the temperatures from D. Grodent et al. (2001); we note that the variability of k is small (T is approximately 700 K at 500 km and 1000 K at 800 km, and this gives very similar values for k in Equation (2): 6.6×10^{-8} cm^3 s^{-1} and 5.2×10^{-8} cm^3 s^{-1}).

The free parameters in the model are thus reduced to two: n_p and the factor f. We fit these parameters to the data extracted from Figure 2 to evaluate the model's performance. To ensure robustness, we also perform a fit using a Markov Chain Monte Carlo (MCMC) method. In Figure 3, we present the results for orbits 13 (panel (a)) and 26 (panel (b)). The best-fit results are shown as dashed lines, while the MCMC density plots are represented in gray. Table 1 provides the fitted values.

We observe good agreement between the data and the model. The reduced χ^2 values for orbits 13 and 26 are $\sim 1 \times 10^{-3}$ mW m^{-2} sr^{-1} and 3×10^{-4} mW m^{-2} sr^{-1}, respectively. The reduced χ^2 is defined as χ^2 divided by the degrees of freedom ν; ν is the number of data points minus the number of free parameters, that is, 5 for orbit 13 and 6 for orbit 26. Although one might not easily distinguish this decay profile from an exponential one at first glance, a best fit with an exponential function yields significantly worse reduced χ^2 values: 2.3×10^{-3} mW m^{-2} sr^{-1} and 5×10^{-4} mW m^{-2} sr^{-1}, respectively.

Figure 4 presents the corner plot for orbit 13, illustrating that the parameters are well constrained. Although there is an evident anticorrelation between n_p and f, this does not significantly impact the results, as the uncertainties are

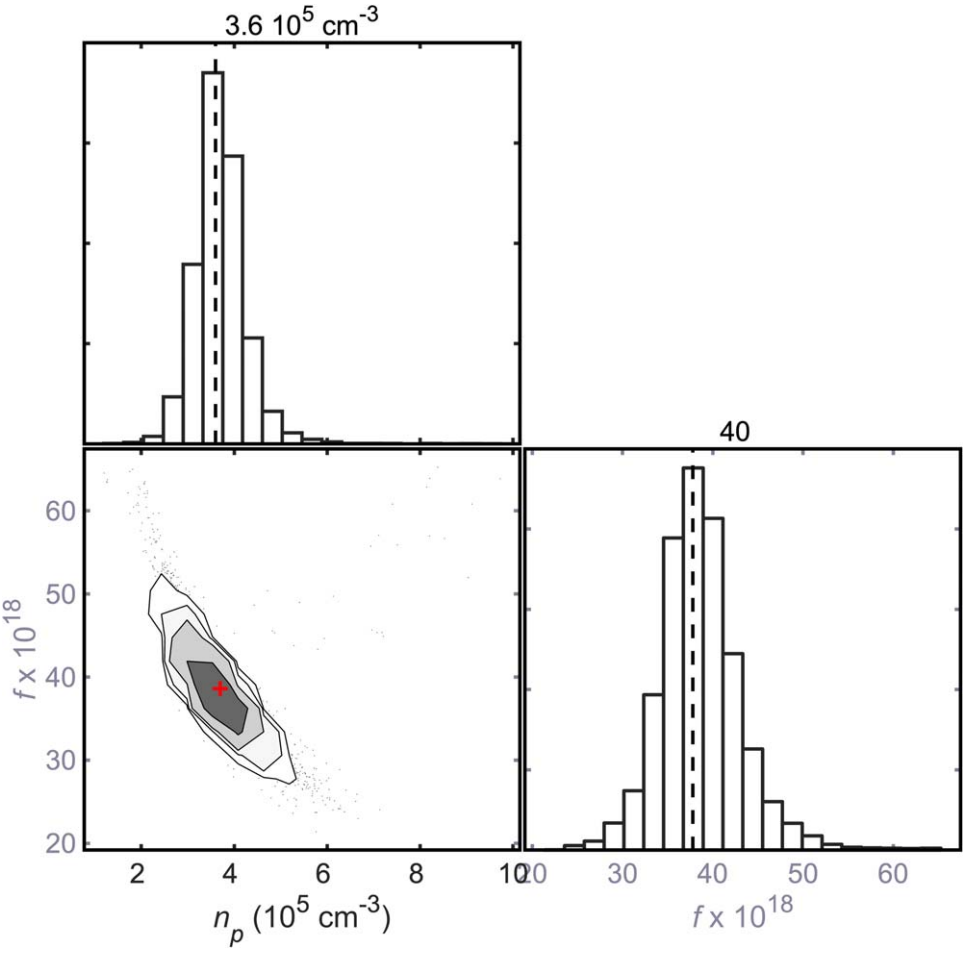

Figure 4. Corner plot for the MCMC model (orbit 13 only). The two diagonal elements show the 1D marginal distributions for the two single parameters, and the off-diagonal element displays 2D projections of the joint distributions between the pair of parameters. The two free parameters are the peak density at $t = 0$ (n_p) and the factor f (units of W m^{-2} sr^{-1} cm^2) that converts from column density to radiance. The numbers above the plots are the median values from the distribution.

reasonably small. Nevertheless, the model is not meant to serve as an absolute method for calculating the column density. The approximately 50% uncertainty in f is acceptable.

This anticorrelation resembles what was observed by B. M. Dinelli et al. (2017) or A. Adriani et al. (2017b) between temperature and column density. What is most remarkable, however, is that the value of f derived solely from the temporal behavior of the radiance—without any additional information beyond electron recombination—aligns very well with values reported in the literature. For instance, B. M. Dinelli et al. (2017) report that a radiance of 1×10^{-4} W m^{-2} sr^{-1} (integrated between 3.35 and 3.75, i.e., similar to the L band) corresponds to a column density of 2×10^{12} cm^{-2}, while a radiance of 1.5×10^{-4} W m^{-2} sr^{-1} corresponds to 3×10^{12} cm^{-2}. This translates to a typical ratio (f) of approximately 50×10^{-18} W m^{-2} sr^{-1} cm^2, which matches our results (ranging from 40 to 80 $\times 10^{-18}$).

The variation in f between the two data sets may be due to statistical fluctuations, given the inherent noise in the data. Moreover, orbit 13 has an emission angle of 52°, while orbit 26 has 33°, potentially introducing an effect related to suboptimal emission angle correction.

In conclusion, the model shows good agreement with the data, demonstrating that it effectively captures the decay behavior of the radiance.

Using the model functions in Figure 3 (dashed lines), it is possible to calculate the half-life as a function of the column density. The result is given in the Appendix (Figure A1). The relationship is an almost perfect hyperbole, and it can be fitted with the following formula:

$$T_{½} = \frac{5 \times 10^{14}}{\mathrm{CD}}, \tag{6}$$

where $T_{½}$ is the half-life in seconds and CD is the column density in cm^{-2}.

5. Discussion and Conclusions

The first notable result of this study is the derivation of the vertical profile of the Io footprints auroral emission in the infrared. The observed vertical profile of the H_3^+ emissions peaks at approximately 600–650 km. In the model of C. Tao et al. (2011), this altitude corresponds to the maximum production rate of H_3^+ caused by monoenergetic electron beams with energies of about 10 keV or higher (C. Tao et al. 2011; Figure 3; see also their Figure 6(b), which directly gives the emission rate). In contrast, beams with energies below 1 keV are inconsistent with our observations. Therefore, JIRAM observations suggest that 10 keV electrons are likely a predominant or at least a significant component of the precipitating population. This finding, however, presents challenges concerning (i) Juno's particle measurements and (ii) the relative altitudes of UV and IR emission peaks.

Juno measurements indicate that the energy distribution is broadband, with a peak between 0.1 and 1 keV (J. R. Szalay et al. 2020), an energy range that does not align with our observations. Regarding the altitude of the IFP as observed in the UV, HST observations of the MAW indicate a peak at 800 km with an FWHM of approximately 850 km (B. Bonfond et al. 2009; B. Bonfond 2010). Similarly, the UV emission of the footprint tail peaks near 900 km, although variations ranging from 700 to 1100 km have been reported. Similar altitudes have been linked to measurements of particle precipitations associated with Io's magnetic shell (J. R. Szalay et al. 2018) based on observations of the IFP tail by Juno-UVS. In summary, UV emissions are observed at higher altitudes than IR, but these altitudes (800 km for UV), as predicted using the model of C. Tao et al. (2011), correspond to electrons with energies between 1 and 10 keV (closer to 1 keV). This is not fully consistent with the estimates we presented.

To address this apparent discrepancy, we propose either that the assumption of (quasi-)monoenergetic beams may not be suitable for modeling the electron precipitation of the IFP or that the temperature vertical profile used in models deviates from the actual one.

Juno's particle measurements reveal broadband distributions (J. R. Szalay et al. 2020), which can produce vertical brightness profiles that differ from the monoenergetic case (B. Benmahi et al. 2024). The vertical extent of the IFP UV brightness also supports the idea that the electron energy distribution is predominantly broadband (Bonfond et al. 2009). As suggested by theoretical efforts (S. L. G. Hess et al. 2010; P. A. Damiano et al. 2019), such energy distribution is associated with precipitating electrons that are accelerated by wave–particle interaction with Alfvén waves. Juno's magnetometer (J. E. P. Connerney et al. 2017) measured intense Alfvénic activity during the crossing of Io's magnetic shell (D. J. Gershman et al. 2019; A. H. Sulaiman et al. 2020), and Juno recorded broadband energy spectra between 0.05 and 30 keV at various distances from the MAW spot along the footprint tail (J. R. Szalay et al. 2018; J. R. Szalay et al. 2020). Furthermore, B. Benmahi et al. (2024) showed that, in the main Jovian aurora, the assumption of monoenergetic electron energy distribution leads to quantitatively different results from a broadband distribution, when the UV auroral emission is used to derive the corresponding precipitating electron energy. We also note that assessing the energy spectrum of precipitating electrons from our IR observations is challenging, as the H_3^+ vertical profile is largely governed by the destruction rate and the temperature profile. Therefore, it is difficult to uniquely determine the source of the discrepancy between the observed relative UV–IR altitude and the one predicted by the model of C. Tao et al. (2011), and we conclude that the discrepancy may arise from the difference between a monoenergetic and a broadband precipitation.

Regardless of the energy of the precipitating electrons, the UV peak being higher than the IR peak presents a distinct challenge. According to C. Tao et al. (2011), for any altitude below 1000 km, the IR peak consistently occurs at a higher altitude than the UV peak. This is because the temperature profile they adopt (from D. Grodent et al. 2001) increases with altitude below 1000 km, causing the IR emission peak to shift to higher altitudes (the IR emission rate is temperature dependent, while the UV one is not; see C. Tao et al. 2011, Figure 7(c)). If the actual temperature profile deviates from this assumption (as discussed in J. N. Yates et al. 2020), the relative positions of the UV and IR peaks might reverse. For instance, the Galileo probe data (A. Seiff et al. 1998, Table 8) indicate the presence of thermal inversion layers.

In summary, while the present observations are somewhat indicative of the presence of high-energy (10 keV) electrons, we suggest that the distribution could be quite broad and that the comparison with the C. Tao et al. (2011) model should be regarded as a qualitative indication rather than a precise constraint. Finally, we note that this unresolved puzzle does not affect our modeling of H_3^+ decay, as the model relies solely on the observed vertical profile of H_3^+ density, independent of the energy distribution of the precipitating electrons.

The second notable result of this study regards the timescale for H_3^+ decay. It is worth noting that an exponential temporal decay is often considered a reasonable approximation, as it combines multiple effects. The electron precipitation does not cease abruptly, but rather diminishes gradually in most cases, and H_3^+ is distributed across different altitudes with varying recombination rates. However, the actual temporal profile better follows a hyperbolic function than an exponential one, and this becomes more evident when electron precipitation rates are variable on short timescales. Understanding this concept is crucial to avoid a common oversimplification: there is no single characteristic timescale for H_3^+ decay. N. Achilleos et al. (1998) estimated the H_3^+ lifetime to be from the tens of seconds in the auroral region to 1000 s in the nonauroral region, S. Miller et al. (2020) report ~100 s, and various other values are reported by T. Stallard et al. (2002), H. Watanabe et al. (2018), and A. Mura et al. (2018): all these values do not contradict the present results but reflect different stages (early or late) of the H_3^+ density decay. This is particularly important when considering comparative measurements between IR and UV emissions (J.-C. Gérard et al. 2018). In fact, IR measurements present two additional complexities: (i) the emission occurs at a different altitude than UV, and (ii) the column density is not directly proportional to the electron flux. Instead, the relationship is nonlinear, as it results from Equation (10) in C. Tao et al. (2011). This favors the detection of lower column densities, revealing details that may not be observable in the UV.

Finally, a remarkable aspect of this study is that we derived both the column density and the factor f (which converts the column density into radiance) solely from the temporal profile of the H_3^+ radiance, finding very good agreement with previous literature. No additional assumptions were made, except for the value of the recombination rate k from G. Sundström et al. (1994). This approach demonstrates the robustness of the model for H_3^+ decay and highlights the unique insights gained from analyzing IR emissions in this context.

6. Open Research

The data used in this study come from Juno and the Jovian Infrared Auroral Mapper (JIRAM) and are publicly available on the Planetary Database System in PDS4 format (A. Adriani 2019). The SPICE bundles used to calibrate the viewing geometry are also publicly available in the Planetary Database System via the Navigation and Ancillary Information Facility (NAIF). The code and the tabulated data are available at doi:10.5281/zenodo.14510369.

Acknowledgments

We thank Agenzia Spaziale Italiana (ASI) for the support of the JIRAM contribution to the Juno mission. This work is funded by the ASI–INAF Addendum No. 2016-23-H.3-2023 to grant 2016-23-H.0. This work was supported by the Fonds de la Recherche Scientifique—FNRS under grant(s) No. T003524F. V.H. acknowledges support from the French government under the France 2030 investment plan, as part of the Initiative d'Excellence d'Aix-Marseille Université—A*MIDEX AMX-22-CPJ-04, as well as support from CNES for the Juno mission.

Appendix

A.1. Instrument

JIRAM is both an imager and a spectrometer in the infrared spectrum (A. Adriani et al. 2008, 2017a). Its imaging channel captures images in two spectral bands, *M* and *L*, using filters positioned over the detector. The imaging channel uses a single detector (266 × 432 pixels) divided into two segments (128 × 432 pixels each) by a nonsensitive strip, with each segment corresponding to a different filter. The *L* band, equipped with a bandpass filter between 3.3 and 3.6 μm, is particularly effective at capturing a significant portion of the infrared H3+ emission (lines at ∼3.3, ∼3.4, and ∼3.55 μm) and assists in reconstructing the context of the measured spectra. JIRAM's spatial resolution is exceptionally high, with an angular resolution of approximately $0\overset{\circ}{.}01$. The *L* band's field of view is $5\overset{\circ}{.}87 \times 1\overset{\circ}{.}74$, with spatial resolution varying based on the spacecraft's distance from the surface, ranging from tens to hundreds of kilometers. The second filter, the *M* band (4.5 to 5 μm), is designed for mapping atmospheric thermal structures.

Images are captured with a time resolution of 1 s, with intervals of 30 s between consecutive images. The *L*-band channel does experience some background noise, likely due to stray light beneath the filter or electronic bleeding within the detector. However, this noise is mitigated using the method described by A. Mura et al. (2017).

A.2. Data Set and Methods

Table A1 gives the list of the JIRAM images used for reconstructing the vertical profile of the Io auroral footprint (Figure 1). The code for the model and the MCMC information are available at a public repository (see A. Mura 2024).

Tables A2 and A3 gives the list of the JIRAM images used for the time variability study. The ROI for orbit 13 is located at ($X_{\mathrm{S\ III}} = 14{,}450$ km, $Y_{\mathrm{S\ III}} = -33{,}880$ km) in the orthographic projection; the ROI for orbit 26 is located at ($X_{\mathrm{S\ III}} = 15{,}690$ km, $Y_{\mathrm{S\ III}} = 20{,}660$ km) in the orthographic projection. The ROI for orbit 13 has been increasingly adjusted with an offset on the *X*-axis of 7 km per observation in order to keep the sub-dot aligned with the center of the ROI. The signal in the ROI for orbit 26 has been adjusted by removing 0.04 mW m^{-2} sr^{-1} to account for a small background signal in the image.

The repository in A. Mura (2024) contains the code for the ionospheric H_3^+ emission as a function of time. The code also contains information on how to implement the variable emission rate (f) function of temperature (see Figure 7(c) of C. Tao et al. 2011). This implementation affects the results (Table 1) by about 10%, so that it is only reported for completeness.

Figure A1 gives the half-life as a function of the column density, as calculated by taking the model functions in Figure 3.

Table A1
Observations Used for Figure 1, Orbit 31

Date	Time	File Name in PDS
2020-12-30	21:05:26.211	JIR_IMG_EDR_2020365T210530_V01.IMG
2020-12-30	21:05:56.290	JIR_IMG_EDR_2020365T210600_V01.IMG
2020-12-30	21:06:26.380	JIR_IMG_EDR_2020365T210630_V01.IMG
2020-12-30	21:06:56.470	JIR_IMG_EDR_2020365T210700_V01.IMG
2020-12-30	21:07:26.559	JIR_IMG_EDR_2020365T210730_V01.IMG
2020-12-30	21:07:56.650	JIR_IMG_EDR_2020365T210800_V01.IMG
2020-12-30	21:08:26.739	JIR_IMG_EDR_2020365T210830_V01.IMG
2020-12-30	21:08:56.831	JIR_IMG_EDR_2020365T210900_V01.IMG
2020-12-30	21:10:56.941	JIR_IMG_EDR_2020365T211101_V01.IMG
2020-12-30	21:11:27.043	JIR_IMG_EDR_2020365T211131_V01.IMG
2020-12-30	21:11:57.136	JIR_IMG_EDR_2020365T211201_V01.IMG
2020-12-30	21:12:27.229	JIR_IMG_EDR_2020365T211231_V01.IMG
2020-12-30	21:12:57.322	JIR_IMG_EDR_2020365T211301_V01.IMG
2020-12-30	21:13:27.415	JIR_IMG_EDR_2020365T211331_V01.IMG
2020-12-30	21:14:57.449	JIR_IMG_EDR_2020365T211501_V01.IMG
2020-12-30	21:15:27.552	JIR_IMG_EDR_2020365T211531_V01.IMG
2020-12-30	21:15:57.647	JIR_IMG_EDR_2020365T211601_V01.IMG
2020-12-30	21:16:27.744	JIR_IMG_EDR_2020365T211631_V01.IMG
2020-12-30	21:16:57.841	JIR_IMG_EDR_2020365T211701_V01.IMG
2020-12-30	21:17:27.939	JIR_IMG_EDR_2020365T211732_V01.IMG
2020-12-30	21:18:57.983	JIR_IMG_EDR_2020365T211902_V01.IMG
2020-12-30	21:19:28.088	JIR_IMG_EDR_2020365T211932_V01.IMG
2020-12-30	21:19:58.187	JIR_IMG_EDR_2020365T212002_V01.IMG
2020-12-30	21:20:28.289	JIR_IMG_EDR_2020365T212032_V01.IMG
2020-12-30	21:20:58.392	JIR_IMG_EDR_2020365T212102_V01.IMG
2020-12-30	21:21:28.495	JIR_IMG_EDR_2020365T212132_V01.IMG
2020-12-30	21:22:58.550	JIR_IMG_EDR_2020365T212302_V01.IMG
2020-12-30	21:23:28.658	JIR_IMG_EDR_2020365T212332_V01.IMG
2020-12-30	21:23:58.764	JIR_IMG_EDR_2020365T212402_V01.IMG
2020-12-30	21:24:28.871	JIR_IMG_EDR_2020365T212433_V01.IMG
2020-12-30	21:24:58.978	JIR_IMG_EDR_2020365T212503_V01.IMG
2020-12-30	21:25:29.088	JIR_IMG_EDR_2020365T212533_V01.IMG

Table A2
Observations Used for Figures 2, 3(a), and 4, Orbit 13

Date	Time	File Name in PDS	Average Radiance in the ROI (mW m^{-2} sr^{-1})
2018-05-24	07:12:27.931	JIR_IMG_EDR_2018144T071232_V01.IMG	0.292
2018-05-24	07:12:58.389	JIR_IMG_EDR_2018144T071302_V01.IMG	0.223
2018-05-24	07:13:28.848	JIR_IMG_EDR_2018144T071333_V01.IMG	0.157
2018-05-24	07:13:59.307	JIR_IMG_EDR_2018144T071403_V01.IMG	0.117
2018-05-24	07:14:29.765	JIR_IMG_EDR_2018144T071433_V01.IMG	0.094
2018-05-24	07:15:00.224	JIR_IMG_EDR_2018144T071504_V01.IMG	0.083
2018-05-24	07:15:30.682	JIR_IMG_EDR_2018144T071534_V01.IMG	0.082

Table A3
Observations Used for Figure 3(b), Orbit 26

Date	Time	File name in PDS	Average radiance in the ROI (mW m^{-2} sr^{-1})
2020-04-10	15:51:40.795	JIR_IMG_EDR_2020101T155144_V01.IMG	0.207
2020-04-10	15:52:10.943	JIR_IMG_EDR_2020101T155215_V01.IMG	0.174
2020-04-10	15:52:41.090	JIR_IMG_EDR_2020101T155245_V01.IMG	0.168
2020-04-10	15:53:11.238	JIR_IMG_EDR_2020101T155315_V01.IMG	0.137
2020-04-10	15:53:41.384	JIR_IMG_EDR_2020101T155345_V01.IMG	0.117
2020-04-10	15:54:11.532	JIR_IMG_EDR_2020101T155415_V01.IMG	0.111
2020-04-10	15:54:41.678	JIR_IMG_EDR_2020101T155445_V01.IMG	0.102
2020-04-10	15:55:11.826	JIR_IMG_EDR_2020101T155515_V01.IMG	0.099

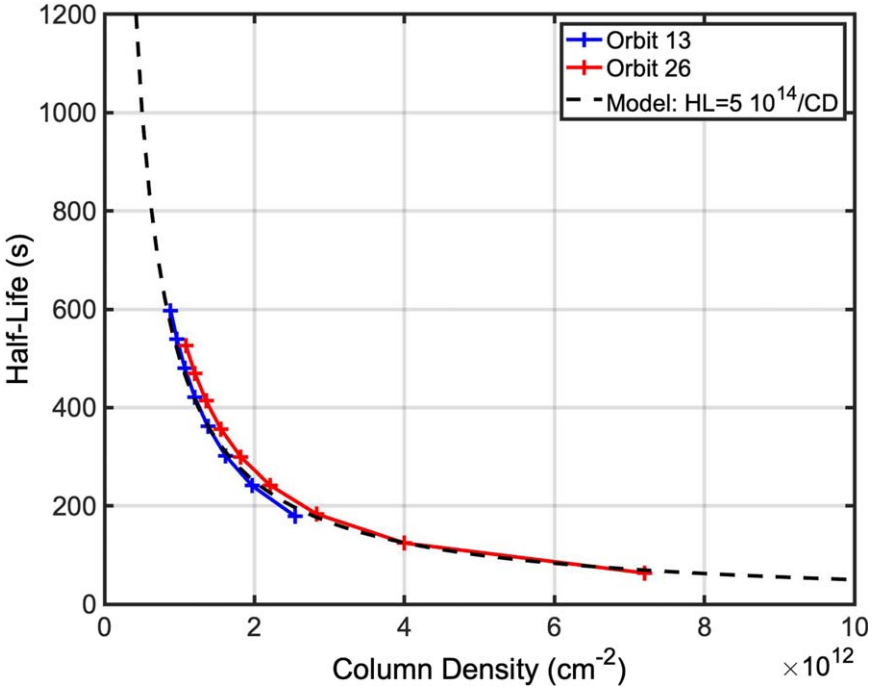

Figure A1. Half-life obtained from the models in Figure 3, as a function the column density. Blue: orbit 13; red: orbit 26; black: analytical formula.

ORCID iDs

A. Mura https://orcid.org/0000-0002-4552-4292
C. Castagnoli https://orcid.org/0000-0001-5396-5306
C. Plainaki https://orcid.org/0000-0003-1483-5052
G. Sindoni https://orcid.org/0000-0002-3348-7930

References

Achilleos, N., Miller, S., Tennyson, J., et al. 1998, JIM: A Time-Dependent, Three-Dimensional Model of Jupiter's Thermosphere and Ionosphere, JGR, 103, 20089
Acuña, M. H., Neubauer, F. M., & Ness, N. F. 1981, Standing Alfvén Wave Current System at Io: Voyager 1 Observations, JGR, 86, 8513
Adriani, A., Coradini, A., Filacchione, G., et al. 2008, JIRAM, The Image Spectrometer in the Near Infrared on Board the Juno Mission to Jupiter, AsBio, 8, 613
Adriani, A., Filacchione, G., Di Iorio, T., Turrini, D., Noschese, R., et al. 2017a, JIRAM, the Jovian Infrared Auroral Mapper, SSRv, 213, 393
Adriani, A., Mura, A., Moriconi, M. L., et al. 2017b, Preliminary JIRAM Results from Juno Polar Observations: 2. Analysis of the Jupiter Southern H_3^+ Emissions and Comparison with the North Aurora, GeoRL, 44, 4633
Adriani, A. 2019, Juno JIRAM Bundle, NASA Planetary Data System, urn:nasa:pds:juno_jiram:1.1, doi:10.17189/1518967
Atreya, S. K., & Donahue, T. M. 1975, The Role of Hydrocarbons in the Lonospheres of the Outer Planets, Icar, 25, 335
Badman, S. V., Branduardi-Raymont, G., Galand, M., et al. 2015, Auroral Processes at the Giant Planets: Energy Deposition, Emission Mechanisms, Morphology and Spectra, SSRv, 187, 99
Belcher, J. W., Goertz, C. K., Sullivan, J. D., & Acuña, M. H. 1981, Plasma Observations of the Alfvén Wave Generated by Io, JGR, 86, 8508
Benmahi, B., Bonfond, B., Benne, B., et al. 2024, Energy Mapping of Jupiter's Auroral Electrons from Juno/UVS Data Using a New H2 UV Emission Mode, A&A, 685, A26
Bolton, S. J., Adriani, A., Adumitroaie, V., et al. 2017, Jupiter's Interior and Deep Atmosphere: The Initial Pole-to-Pole Passes with the Juno Spacecraft, Sci, 356, 821
Bonfond, B. 2010, The 3D Extent of the Io UV Footprint on Jupiter, JGRA, 115, A09217
Bonfond, B., Grodent, D., Gérard, J-C., et al. 2008, UV Io Footprint Leading Spot: A Key Feature for Understanding the UV Io Footprint Multiplicity?, GeoRL, 35, L05107
Bonfond, B., Grodent, D., Gérard, J-C., et al. 2009, The Io UV Footprint: Location, Inter-spot Distances and Tail Vertical Extent, JGRA, 114, A07224
Bonfond, B., Saur, J., Grodent, D., et al. 2017, The Tails of the Satellite Auroral Footprints at Jupiter, JGRA, 122, 7985
Clarke, J. T., Ballester, G. E., Trauger, J., et al. 1996, Far-Ultraviolet Imaging of Jupiter's Aurora and the Io Footprint, Sci, 274, 404
Clarke, J. T., Ballester, G., Trauger, J., et al. 1998, Hubble Space Telescope Imaging of Jupiter's UV Aurora During the Galileo Orbiter Mission, JGR, 103, 20217
Connerney, J. E. P., Baron, R., Satoh, T., & Owen, T. 1993, Images of Excited H_3^+ at the Foot of the Io Flux Tube in Jupiter's Atmosphere, Sci, 262, 1035
Connerney, J. E. P., Benn, M., Bjarno, J. B., et al. 2017, The Juno Magnetic Field Investigation, SSRv, 213, 39
Connerney, J. E. P., Kotsiaros, S., Oliversen, R. J., et al. 2018, A New Model of Jupiter's Magnetic Field from Juno's First Nine Orbits, GeoRL, 45, 2590
Connerney, J. E. P., & Satoh, T. 2000, The H_3^+ Ion: A Remote Diagnostic of the Jovian Magnetosphere, RSPTA, 358, 2471
Damiano, P. A., Delamere, P. A., Stauffer, B., Ng, C-S., & Johnson, J. R. 2019, Kinetic Simulations of Electron Acceleration by Dispersive Scale Alfvén Waves in Jupiter's Magnetosphere, GeoRL, 46, 3043
Dinelli, B. M., Miller, S., & Tennyson, J. 1992, Bands of H_3^+ up to $4\nu_2$: Rovibrational Transitions from First Principles calculations, JMoSp, 153, 718
Dinelli, B. M., Fabiano, F., Adriani, A., et al. 2017, Preliminary JIRAM Results from Juno Polar Observations: 1. Methodology and Analysis Applied to the Jovian Northern Polar Region, GeoRL, 44, 4625
Dinelli, B. M., Le Sueur, C. R., Tennyson, J., & Amos, R. D. 1995, Ab Initio Ro-vibrational Levels of H_3^+ beyond the Born–Oppenheimer Approximation, CPL, 232, 295
Drossart, P., Maillard, J., Caldwell, J., et al. 1989, Detection of H_3^+ on Jupiter, Natur, 340, 539
Gérard, J-C., Mura, A., Bonfond, B., et al. 2018, Concurrent Ultraviolet and Infrared Observations of the North Jovian Aurora during Juno's First Perijove, Icar, 312, 145
Gershman, D. J., Connerney, J. E. P., Kotsiaros, S., et al. 2019, Alfvénic Fluctuations Associated with Jupiter's Auroral Emissions, GeoRL, 46, 7157
Grodent, D., Waite, J. H., & Gérard, J.-C. 2001, A Self-consistent Model of the Jovian Auroral Thermal Structure, JGR, 106, 12933
Gurnett, D. A., & Goertz, C. K. 1981, Multiple Alfvén Wave Reflections Excited by Io: Origin of the Jovian Decametric Arcs, JGR, 86, 717
Hess, S. L. G., Delamere, P., Dols, V., Bonfond, B., & Swift, D. 2010, Power Transmission and Particle Acceleration along the Io Flux Tube, JGRA, 115, A06205
Hue, V., Gladstone, G. R., Louis, C. K., et al. 2023, The Io, Europa, and Ganymede Auroral Footprints at Jupiter in the Ultraviolet: Positions and Equatorial Lead Angles, JGRA, 128, e2023JA031363

Hue, V., Szalay, J. R., Greathouse, T. K., et al. 2022, A Comprehensive Set of Juno in Situ and Remote Sensing Observations of the Ganymede Auroral Footprint, GeoRL, 49, e2021GL096994
Huntress, W. T., Jr. 1975, A Review of Jovian Ionospheric Chemistry, AdAMP, 10, 295
Huntress, W. T., Jr. 1977, Laboratory Studies of Bimolecular Reactions of Positive Ions in Interstellar Clouds, in Comets, and in Planetary Atmospheres of Reducing Composition, ApJS, 33, 495
Ingersoll, A. P., Vasavada, A. R., Little, B., et al. 1998, Imaging Jupiter's Aurora at Visible Wavelengths, Icar, 135, 251
Johnson, R. E., Stallard, T. S., Melin, H., Nichols, J. D., & Cowley, S. W. H. 2017, Jupiter's Polar Ionospheric Flows: High Resolution Mapping of Spectral Intensity and Line-of-Sight Velocity of H3 + ions, JGRA, 122, 7599
Kivelson, M., Bagenal, F., Kurth, W., et al. 2004, Magnetospheric Interactions with Satellites, Jupiter. The Planet, Satellites and Magnetosphere. (Cambridge: Cambridge Univ. Press), 513
Lam, H. A., Miller, S., Joseph, R. D., et al. 1997, Variation in the H_3^+ Emission of Uranus, ApJ, 474, L73
Larsson, M. 2012, Dissociative Recombination of H_3^+: 10 Years in Retrospectphil, RSPTA, 370, 5118
Larsson, M., McCall, B. J., & Orel, A. E. 2008, The Dissociative Recombination of H_3^+—a Saga Coming to an End?, CPL, 462, 145
Lystrup, M. B., Miller, S., Dello Russo, N., Vervack Jr, R. J., & Stallard, T. 2008, First Vertical Ion Density Profile in Jupiter's Auroral Atmosphere: Direct Observations Using the Keck II Telescope, ApJ, 677, 790
Maillard, J. P., Lellouch, E., Waite, J. H., et al. 1999, Search for Ionospheric Winds in Jupiter from the H3+ Emissions, BAAS, 31, 1186
Melin, H., Miller, S., Stallard, T., & Grodent, D. 2005, Non-LTE Effects on H_3^+ Emission in the Jovian Upper Atmosphere, Icar, 178, 97
Migliorini, A., Dinelli, B. M., Castagnoli, C., et al. 2023, First Observations of CH4 and Spatially Resolved Emission Layers at Jupiter Equator, as Seen by JIRAM/Juno, JGRE, 128, e2022JE007509
Migliorini, A., Dinelli, B. M., Moriconi, M. L., et al. 2019, H_3^+ Characteristics in the Jupiter Atmosphere as Observed at Limb with Juno/JIRAM, Icar, 329, 132
Miller, S., Achilleos, N., Ballester, G. E., et al. 1997, Mid-to-Low Latitude H +3Emission from Jupiter, Icar, 130, 57
Miller, S., Tennyson, J., Geballe, T. R., & Stallard, T. 2020, Thirty Years of H_3^+ Astronomy, RvMP, 92, 035003
Moirano, A., Mura, A., Adriani, A., et al. 2021, Morphology of the Auroral Tail of Io, Europa, and Ganymede from JIRAM L-band Imager, JGRA, 126, e2021JA029450
Moirano, A., Mura, A., Bonfond, B., et al. 2023, Variability of the Auroral Footprint of Io Detected by Juno-JIRAM and Modeling of the Io Plasma Torus, JGRA, 128, e2023JA031288
Moriconi, M. L., et al. 2017, Preliminary JIRAM Results from Juno Polar Observations: 3. Evidence of Diffuse Methane Presence in the Jupiter Auroral Regions, GeoRL, 44, 4641
Mura, A. 2024, Data and Code for 'Vertical and Temporal H3+ Structure at the Auroral Footprint of Io', v2, Zenodo, doi:10.5281/zenodo.14510369
Mura, A., Adriani, A., Altieri, F., et al. 2017, Infrared Observations of Jovian Aurora from Juno's First Orbits: Main Oval and Satellite Footprints: Jovian Aurora IR Observations from Juno, GeoRL, 44, 5308
Mura, A., Adriani, A., Connerney, J. E. P., et al. 2018, Juno Observations of Spot Structures and a Split Tail in Io-Induced Aurorae on Jupiter, Sci, 361, 774
Neubauer, F. 1980, Nonlinear Standing Alfvén Wave Current System at Io: Theory, JGR, 85, 1171
Oka, T. 1980, Observation of the Infrared Spectrum of H+3, PhRvL, 45, 531
Perry, J. J., Kim, Y. H., Fox, J. L., & Porter, H. S. 1999, Chemistry of the Jovian Auroral Ionosphere, JGR, 104, 16541
Rabia, J., Hue, V., André, N., et al. 2024, Properties of Electrons Accelerated by the Ganymede–Magnetosphere Interaction: Survey of Juno High-Latitude Observations, JGRA, 129, e2024JA032604
Rabia, J., Hue, V., Szalay, J. R., et al. 2023, Evidence for Non-monotonic and Broadband Electron Distributions in the Europa Footprint Tail Revealed by Juno In Situ Measurements, GeoRL, 50, e2023GL103131
Rego, D., Achilleos, N., Stallard, T., et al. 1999, Supersonic Winds in Jupiter's Aurorae, Natur, 399, 121
Sánchez-López, A., López-Puertas, M., García-Comas, M., et al. 2022, The CH4 Abundance in Jupiter's Upper Atmosphere, A&A, 662, A91
Schlegel, S., & Saur, J. 2022, Alternating Emission Features in Io's Footprint Tail: Magnetohydrodynamical Simulations of Possible Causes, JGRA, 127, e2021JA030243
Seiff, A., Kirk, D. B., Knight, T. C. D., et al. 1998, Thermal Structure of Jupiter's Atmosphere near the Edge of a 5-μm Hot Spot in the North Equatorial Belt, JGR, 103, 22857
Stallard, T., Miller, S., Millward, G., & Joseph, R. D. 2001, On the Dynamics of the Jovian Ionosphere and Thermosphere: I. The Measurement of Ion Winds, Icar, 154, 475
Stallard, T., Miller, S., Millward, G., & Joseph, R. D. 2002, On the Dynamics of the Jovian Ionosphere and Thermosphere: II. The Measurement of H_3^+ Vibrational Temperature, Column Density, and Total Emission, Icar, 156, 498
Stallard, T. S., Melin, H., Miller, S., et al. 2015, Cassini VIMS Observations of H_3^+ Emission on the Nightside of Jupiter, JGRA, 120, 6948
Sulaiman, A. H., Hospodarsky, G. B., Elliott, S. S., et al. 2020, Wave–Particle Interactions Associated with Io's Auroral Footprint: Evidence of Alfvén, Ion Cyclotron, and Whistler Modes, GeoRL, 47, e2020GL088432
Sundström, G., Mowat, J. R., Danared, H., et al. 1994, Destruction Rate of H3 + by Low-Energy Electrons Measured in a Storage-Ring Experiment, Sci, 263, 785
Szalay, J. R., Allegrini, F., Bagenal, F., et al. 2020, A New Framework to Explain Changes in Io's Footprint Tail Electron Fluxes, GeoRL, 47, e2020GL089267
Szalay, J. R., Bonfond, B., Allegrini, F., et al. 2018, In Situ Observations Connected to the Io Footprint Tail Aurora, JGRE, 123, 3061
Tao, C., Badman, S. V., & Fujimoto, M. 2011, UV and IR Auroral Emission Model for the Outer Planets: Jupiter and Saturn Comparison, Icar, 213, 581
Uno, T., Kasaba, Y., Tao, C., et al. 2015, Vertical Emissivity Profiles of Jupiter's Northern H_3^+ and H2 Infrared Auroras Observed by Subaru/IRCS, JGRA, 119, 10,219
Vasavada, A. R., Bouchez, A. H., Ingersoll, A. P., Little, B., & Anger, C. D. 1999, Jupiter's Visible Aurora and Io Footprint, JGR, 104, 27133
von Kármán, T. 1911, Ueber den Mechanismus des Widerstandes, Den Ein Bewegter Körper in einer Flüssigkeit Erfährt, NWGot, 1911, 509, http://eudml.org/doc/58812
Waite, J. H., Jr, Cravens, T. E., Kozyra, J., et al. 1983, Electron Precipitation and Related Aeronomy of the Jovian Thermosphere and Ionosphere, JGR, 88, 6143
Watanabe, H., Kita, H., Tao, C., et al. 2018, Pulsation Characteristics of Jovian Infrared Northern Aurora Observed by the Subaru IRCS with Adaptive Optics, GeoRL, 45, 11,547
Yates, J. N., Ray, L. C., Achilleos, N., Witasse, O. G., & Altobelli, N. 2020, Magnetosphere–Ionosphere–Thermosphere Coupling at Jupiter Using a Three-Dimensional Atmospheric General Circulation Model, JGRA, 125, e2019JA026792
Zarka, P. 2004, Fast Radio Imaging of Jupiter's Magnetosphere at Low-Frequencies with LOFAR, P&SS, 52, 1455